RSC Advances

PAPER

View Article Online
View Journal | View Issue

Cite this: *RSC Adv.*, 2024, **14**, 36471

Preparation of a lithium–sulfur battery diaphragm catalyst and its battery performance

Jiayi Ren and Qihao Zhao *

Lithium–sulfur batteries (LSBs) with metal lithium as the anode and elemental sulfur as the cathode active materials have attracted extensive attention due to their high theoretical specific capacity (1675 mA h g^{-1}), high theoretical energy density (2600 W h kg^{-1}), low cost, and environmental friendliness. However, the discharge intermediate lithium polysulfide undergoes a shuttle side reaction between the two electrodes, resulting in low utilization of the active substances. This limits the capacity and cycle life of LSBs and further delays their commercial development. However, the number of active sites and electron transport capacity of such catalysts still do not meet the practical development needs of lithium–sulfur batteries. In view of these issues, this paper focuses on a zinc–cobalt compound catalyst, modifying it through heteroatom doping, bimetallic synergistic effect and heterogeneous structure design to enhance the performance of LSBs as a separator modification material. A carbon shell-supported boron-doped ZnS/CoS_2 heterojunction catalytic material (B–ZnS/CoS_2@CS) was prepared, and its performance in lithium–sulfur batteries was evaluated. A carbon substrate (CS) was prepared by pyrolysis of sodium citrate, and the boron-doped ZnS/CoS_2 heterojunction catalyst was formed on the CS using a one-step solvothermal method. The unique heterogeneous interface provides numerous active sites for the adsorption and catalysis of polysulfides. The uniformly doped, electron-deficient boron further enhances the Lewis acidity of the ZnS/CoS_2 heterojunction, while also regulating electron transport. The B–ZnS/CoS_2@CS catalyst effectively inhibits the diffusion of LiPS anions by utilizing additional lone-pair electrons. The lithium–sulfur battery using the catalyst-modified separator achieves a high specific capacity of 1241 mA h g^{-1} at a current density of 0.2C and retains a specific capacity of 384.2 mA h g^{-1} at 6.0C. In summary, B–ZnS/CoS_2@CS heterojunction catalysts were prepared through boron doping modification. They can promote the conversion of polysulfides and effectively inhibit the shuttle effect. The findings provide valuable insights for the future modification and preparation of lithium–sulfur battery catalysts.

Received 4th September 2024
Accepted 28th October 2024

DOI: 10.1039/d4ra06366j

rsc.li/rsc-advances

1. Introduction

With the "dual-carbon" goal proposed by the state in 2020, there has been an increasing trend toward transitioning from traditional fossil energy to green and low-carbon energy. Prior to this, the lithium-ion battery (LIB) system had attracted considerable attention as a new energy technology, being used in portable mobile devices like cell phone rechargeable batteries, as well as in national defense technologies such as missiles and satellites.[1] However, the low energy density (150–200 W h kg^{-1}) limits the further development of LIBs.[2–4] This creates an urgent need to develop energy storage devices with higher energy densities. Among them, lithium–sulfur batteries (LSBs) have become a strong contender after lithium-ion batteries due to their higher theoretical energy density (2600 W h kg^{-1}) and theoretical specific capacity (1675 mA h g^{-1}).[5–11]

Conventional LSBs are composed of a sulfur-based cathode, a porous diaphragm, a lithium anode, and an organic electrolyte.[12–18] Among them, the sulfur-based cathode serves as the reaction center, and a complex of sulfur powder and carbon material is generally used as the main ingredient. The porous diaphragm serves as the medium for blocking the cathode and anode, and is usually an electrically insulating polyolefin-type diaphragm. The lithium anode is a commercially available lithium metal wafer. Finally, the electrolyte is usually an ether electrolyte with added lithium salts. Unlike the energy storage mechanism of lithium-ion batteries, the charging and discharging process of LSBs is more complex and involves a solid–liquid–solid phase transition process.[9,10,13,14,19,20]

The total equation for the sulfur reduction reaction (SRR) of LSBs during discharge is:

$$S_8 + 16Li \rightarrow 8Li_2S$$

School of Chemical, Marine and Life Sciences, Dalian University of Technology, Dalian 116023, China. E-mail: 18641157899@163.com

The sulfur is in an unlithiated state when the battery is in its initial state, *i.e.*, the initial state of the reaction is the discharge process. The specific reaction is mainly divided into four stages as follows.

$$\text{Stage I: } S_8\ (s) \rightarrow Li_2S_8\ (l)$$

$$\text{Stage II: } Li_2S_8\ (l) \rightarrow Li_2S_6\ (l)/Li_2S_4\ (l)$$

$$\text{Stage III: } Li_2S_4\ (l) \rightarrow Li_2S_2\ (s)/Li_2S\ (s)$$

$$\text{Stage IV: } Li_2S_2\ (s) \rightarrow Li_2S\ (s)$$

Lithium–sulfur batteries are expected to be the next-generation alternative for energy storage systems due to its many advantages, including higher theoretical energy density, and abundant and low-cost sulfur materials. However, there are still many challenges to solve in practical application,[21–24] including the following aspects:

(1) The electronic insulating properties of sulfur and its final discharge products.[25–27] The electrical conductivity of sulfur at room temperature is 5×10^{-30} S cm^{-1} and that of Li_2S_2/Li_2S is 3.6×10^{-7} S cm^{-1}. The lower electron transport capacity leads to an increase in the polarization of the electrochemical reaction. Consequently, the deposition of the passivation layer causes irreversible loss of the active material.

(2) Shuttle effect.[28] In the sulfur reduction process, the long-chain polysulfides in the liquid phase of the electrolyte pass through the diaphragm into the negative electrode under the effect of a concentration gradient to react with lithium and further generate short-chain polysulfides. Under the continuous reaction, the short-chain polysulfide diffuses back to the positive electrode to carry out charging and the oxidation reaction under the impetus of the concentration gradient, and generates a long-chain polysulfide. The phenomenon is called the "shuttle effect" (Fig. 2b). This phenomenon leads to corrosion of the lithium anode and poor cycle reversibility, affecting the battery life.

(3) Volume expansion[29] The large density difference between S (2.07 g cm^{-1}) and Li_2S (1.66 g cm^{-1}) results in a volume change of about 80% inside the battery. With the continuing battery charging and discharging process, the large volume change will cause the anode carbon and sulfur composite structure to form a gap, which further affects the sulfur utilization rate.

(4) Safety hazards caused by lithium dendrites.[15] Generally speaking, the uneven surface of the lithium anode, along with the non-uniform distribution of lithium ions and current, leads to uneven deposition. This results in the continuous growth of lithium dendrites, which can penetrate through the diaphragm, causing an internal short circuit in the battery and posing potential safety hazards.

In response to the above problems, researchers have developed many solutions, including the design of porous carbon structures with the appropriate pore size,[30] anode composite catalyst materials,[31] modified binders,[32] electrolyte additives,[33–36] and the assembly of solid-state electrolyte batteries.[37] Compared to the above measures, the utilization of catalyst-modified diaphragms has attracted a lot of attention from researchers due to its advantages, such as simple experimental manipulation, as well as significant performance improvement.

Metal sulfides have good potential for applications in the field of LSBs because of their higher room temperature conductivity, but a single catalytic active site is still insufficient for them to realize the catalytic conversion of a large number of LiPSs. Bimetallic sulfide heterostructures have a unique role in catalyzing LiPSs because of their ability to expose more active sites due to interfacial coupling. For example, Lee and colleagues[38] reported on a CoS_2/Fe_7S_8/NG heterostructure, in which a strong built-in electric field was spontaneously generated at the contact interface between the two, owing to the equilibrium tendency of the Fermi energy levels, which greatly accelerated the electron transfer ability and LiPSs adsorption ability. However, the catalytic effect of heterostructures is not limited to this. Furthermore, the design of defective heterostructures to expose a richer variety of active sites based on interfacial engineering to achieve a higher level of battery performance has been demonstrated by researchers.

A one-step hydrothermal method was used to synthesize carbon-shell-bearing boron-doped ZnS/CoS_2 heterojunction catalysts (B–ZnS/CoS_2@CS) using carbon shells (CS) as substrates. The fabricated catalysts better retained the carbon shell structure, which was favorable for the transport of electrons and ions inside the LSBs, and this advantage was further amplified by the uniform introduction of electron-deficient B atoms and the construction of the internal electric field. Meanwhile, the lattice of the ZnS/CoS_2 heterostructure modified by boron atoms was distorted, exposing more active sites. Combining the strong adsorption ability of CoS_2 and the high catalytic activity of ZnS, the LSBs assembled with the B–ZnS/CoS_2@CS-modified septa exhibited superior cycling performance. With 1500 cycles at 2.0C and a capacity decay rate of 0.043% per cycle, the cells maintained a high area-specific capacity of 6.22 mA h cm^{-2} after 120 cycles at 0.2C even under the harsh conditions of a liquid–sulfur ratio (E/S) of 8 μl mg^{-1} and a sulfur loading of 6.14 mg cm^{-2}.

2. Experimental section

2.1 Preparation of carbon shells (CS)

5 g of sodium citrate was dried in an oven at 155 °C for 24 h and fully ground. The white powder was then placed in a porcelain boat, annealed in a tube furnace under argon atmosphere at a heating rate of 5 °C min^{-1}, and held at 800 °C for 1 h. The product was collected by natural cooling to room temperature. The products were then stirred in 3 M hydrochloric acid solution for 6 h, and washed with large amounts of deionized water. The black carbon shell powder was collected after 12 h of freeze-drying.

2.2 Preparation of B–ZnS/CoS_2@CS catalysts

100 mg of CS powder was taken in a mixture of 30 ml of deionized water and 30 ml of ethylene glycol, and dispersed by

ultrasonication for 1 h. Then, 0.297 g of $Zn(NO_3)_2 \cdot 6H_2O$ and 0.582 g of $Co(NO_3)_2 \cdot 6H_2O$ were added and continued to be ultrasonicated for 30 min. Subsequently, 0.24 g of urea and 0.3 g of thioacetamide were added to the above solution and stirred for 30 min. After that, 5 mmol of boric acid was added to the solution with continuous stirring for 1 h, and then it was transferred into a 100 ml high-pressure hydrothermal kettle. The reaction was carried out in an autoclave at 180 °C for 24 h. After cooling to room temperature, the product was washed by centrifugation for 3–5 times, and the black powder of B–ZnS/CoS_2@CS was collected after freeze-drying for 24 h (also noted as B–ZnS/CoS_2@CS). When the addition of boric acid was 1 mmol and 20 mmol, the products were noted as 1B–ZnS/CoS_2@CS and 3B–ZnS/CoS_2@CS, respectively.

2.3 Preparation of ZnS/CoS_2@CS catalysts

The preparation process of ZnS/CoS_2@CS and B–ZnS/CoS_2@CS is basically the same. The difference is that no boric acid dopant is added, and the same freeze-drying treatment is used at the end.

3. Results and discussion

3.1 The synthesis route of the catalyst is shown in Fig. 1

After first obtaining the sheet CS material by simple high-temperature annealing treatment, the ZnS/CoS_2 heterojunction catalyst was stretched onto the CS by solvothermal method. To further enhance the catalytic ability of this heterojunction, boric acid was introduced for boron doping to form B–ZnS/CoS_2@CS, which was used for the diaphragm modification of the lithium–sulfur batteries.

The CS morphology obtained using annealing is shown in Fig. 2a, where the material shows a stacked lamellar structure. Thus, the longer ultrasonic dispersion was carried out while stretcher-loading the catalyst. The corresponding XRD results are shown in Fig. 2b, where two distinct diffraction peaks, representing the (0 0 2) and (1 0 1) crystalline surfaces of the graphitic carbon, are shown at approximately 25.3° and 43.8° diffraction angles, respectively.[39–42]

The morphology of the ZnS/CoS_2@CS catalyst obtained by solvothermal method is shown in Fig. 3a. It can be observed

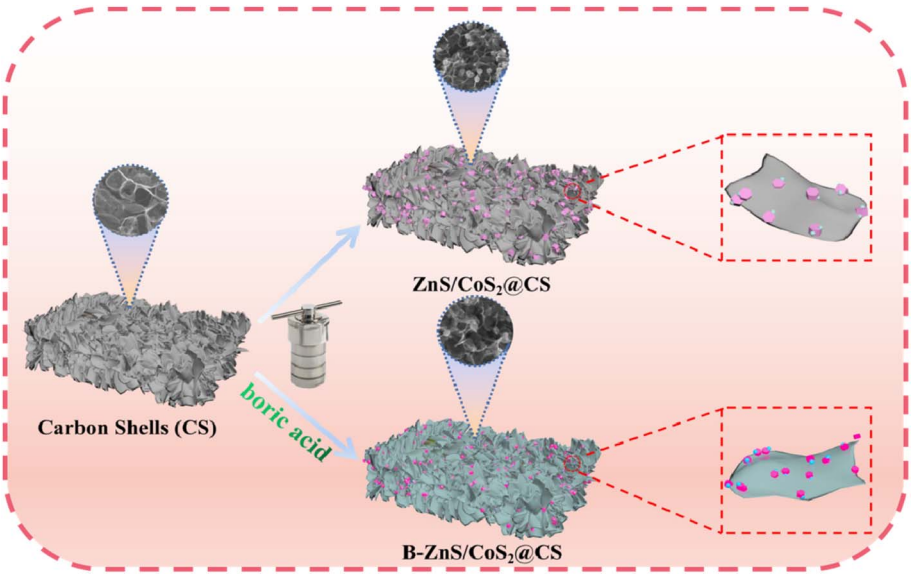

Fig. 1 The schematic diagram of the preparation process of B–ZnS/CoS_2@CS.

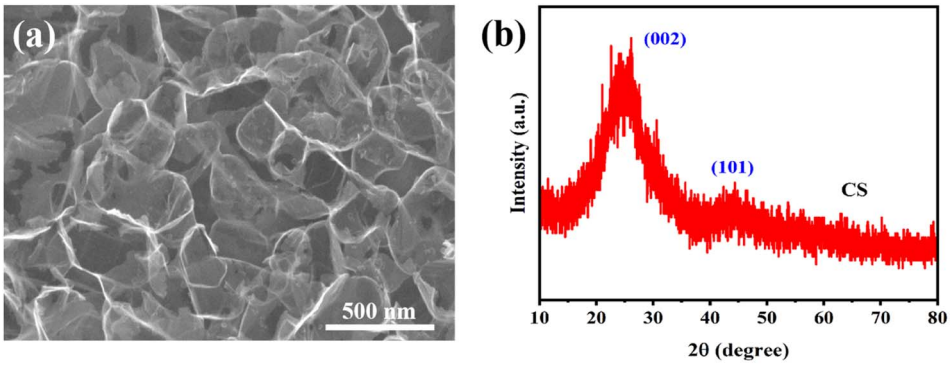

Fig. 2 The morphology and phase structure of CS: (a) SEM and (b) XRD result.

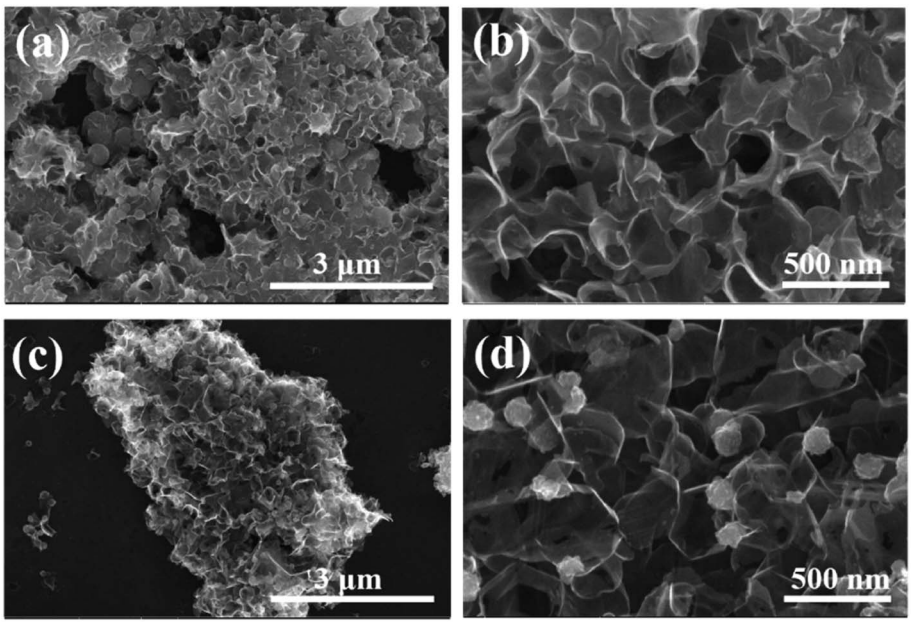

Fig. 3 SEM images of the catalytic materials: (a and b) ZnS/CoS_2@CS and (c and d) B–ZnS/CoS_2@CS.

that many nanospheres are distributed between the lamellar CS layers, indicating the successful loading of the catalyst. However, the accumulation of small spheres is serious, which reduces the specific surface area of CS to some extent and is not favorable for the adsorption of polysulfides. Notably, after boron doping of the catalyst, as shown in Fig. 3c, the morphology of B–ZnS/CoS_2@CS still shows a sheet-like structure without obvious stacking and changes. Meanwhile, from

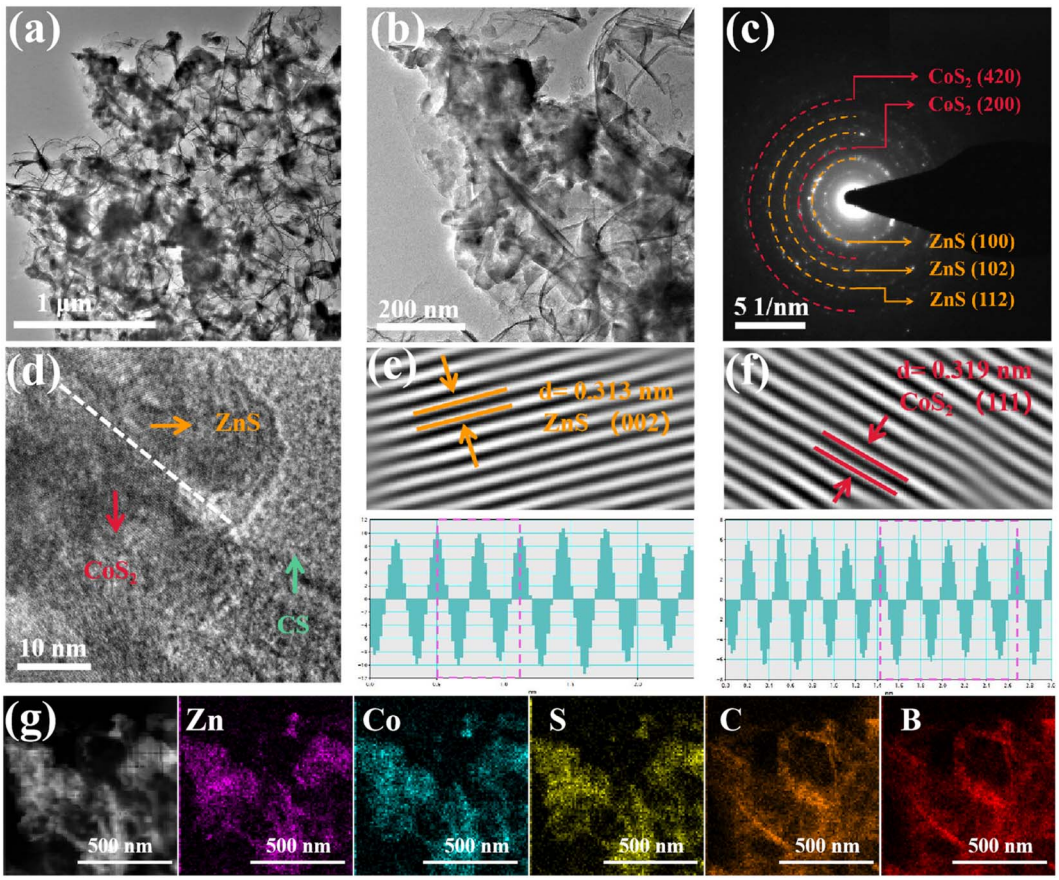

Fig. 4 (a and b) TEM image, (c) SAED pattern, (d–f) HRTEM image of B–ZnS/CoS_2@CS, and (g) EDX mapping results.

Fig. 3d, it is found that the catalyst spheres are more uniformly distributed, in which the size of the spheres is reduced to approximately 125 nm. This suggests that boron doping facilitates the increase of the specific surface area of the material, further exposing more polysulfide sulfide adsorption and catalytic sites.

The TEM of the catalyst is shown in Fig. 4. It can be observed that the morphology of the catalysts (Fig. 4a and b) is consistent with the SEM photographs, showing a thin sheet structure and uniformly distributed catalysts. In addition, the SAED plots in Fig. 4c show diffraction rings corresponding to the ZnS (1 0 0), ZnS (1 0 2), ZnS (1 1 2), CoS_2 (2 0 0) and CoS_2 (4 2 0) planes, respectively, confirming the polycrystalline nature of B–ZnS/CoS_2@CS. To further investigate the microstructure of the B–ZnS/CoS_2@CS catalysts, HRTEM observation and analysis were carried out. Distinguishable lattice stripes belonging to ZnS and CoS_2, as well as disordered regions belonging to CS, were observed from Fig. 4d. Meanwhile, by applying the discrete Fourier transform (FFT) to the different lattice regions, the polycrystalline nature of the catalysts was confirmed in the diffracted rings, corresponding to ZnS (0.313 nm) and CoS_2 (0.319 nm) with different degrees of local lattice distortion at the lattice stripe spacing. This suggests that boron doping can interfere with the lattice structure of the catalysts, favoring the creation of defects and exposing more catalytically active sites.[43–46] Fig. 4g shows that Zn, Co, S, C and B elements are uniformly distributed on B–ZnS/CoS_2@CS, further indicating the uniform introduction of boron.

The XRD test results of the catalyst are shown in Fig. 5a. The samples before and after doping corresponded to the ZnS crystalline phase (PDF # 36-1450) and CoS_2 crystalline phase (PDF # 41-1471). Together with the TEM images, these results indicated the successful preparation of the heterojunction catalysts. It was also observed that after the catalyst was loaded onto the carbon substrate, the characteristic peak of the (0 0 2) crystalline plane belonging to graphitic carbon was shifted left to 21.68°. The layer spacing of the CS was also calculated from Bragg's equation to increase from 0.35 to 0.41 nm, which was attributed to the loading of the catalyst on the CS. In addition, B–ZnS/CoS_2@CS shows weaker intensity of carbon characteristic peaks, indicating that the carbon becomes less crystalline and more defective after boron doping. As shown in the Raman spectra of Fig. 5b, the different catalysts show obvious characteristic peaks (D and G peaks) at 1342 cm^{-1} and 1578 cm^{-1}. The CS : ZnS/CoS_2@CS : B–ZnS/CoS_2@CS I_D/I_G ratios are 1.27, 1.49 and 1.53, and were calculated based on the fitting results. These results further proved that the boron doping exposed more defective sites in the catalysts, which would be favorable for the sulfur reduction–oxidation reaction. Notably, the Raman spectrum of the B–ZnS/CoS_2@CS catalyst was found to display

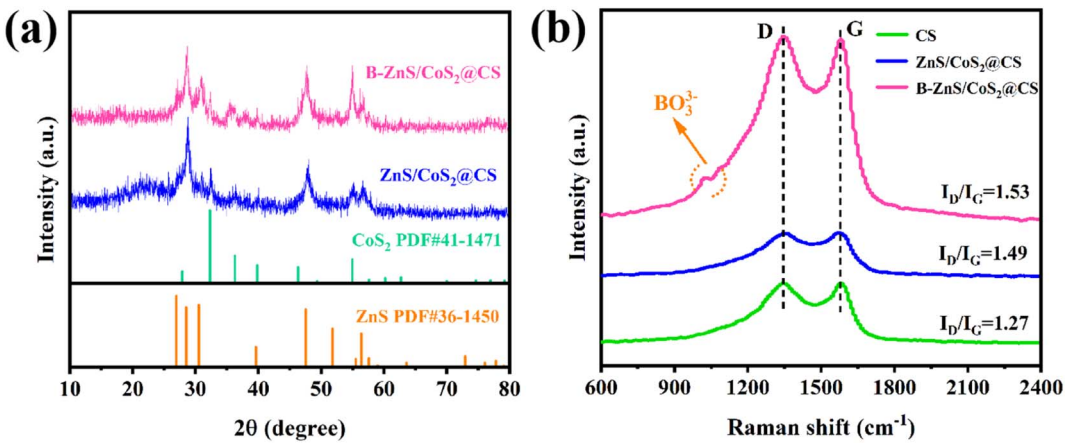

Fig. 5 Physical properties of different catalysts: (a) XRD and (b) Raman results.

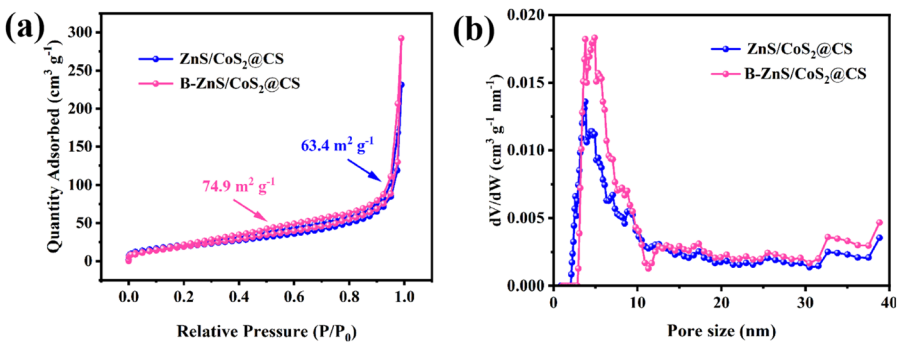

Fig. 6 Pore structure of ZnS/CoS_2@CS and B–ZnS/CoS_2@CS: (a) N_2 adsorption–desorption curve and (b) pore size distribution.

a characteristic peak at 1020 cm^{-1}, which may be the characteristic peak of the BO_3^{3-} species.

The N_2 adsorption and desorption curves of the catalysts are shown in Fig. 6a. As seen, the specific surface areas of the catalysts before and after doping were 63.4 $m^2 g^{-1}$ and 74.9 $m^2 g^{-1}$, respectively. The specific surface area of the B–ZnS/CoS_2@CS catalyst was slightly higher than that of the ZnS/CoS_2@CS, suggesting that more polysulfide adsorption and catalytically active sites were exposed by the B–ZnS/CoS_2@CS catalyst, which agreed with the analytical results of SEM. In addition, the pore sizes of the two catalysts were mainly concentrated at 2–40 nm with a mesoporous structure (Fig. 6b). The pore structure of the B–ZnS/CoS_2@CS catalyst was more distributed in this interval, which was conducive to the selective transmission of ions and improvement of the physical properties of the modified diaphragm to reduce the cell polarization.[47–49]

Further analysis of the chemical states of the boron-doped heterojunction catalysts was carried out by XPS. The Zn 2p XPS of the ZnS/CoS_2@CS and B–ZnS/CoS_2@CS catalysts are shown in Fig. 7a. After boron doping, the binding energies of the $2p_{3/2}$ and $2p_{1/2}$ characteristic peaks of Zn were changed from 1022.73 eV and 1045.75 eV, respectively, to 1022.50 eV and 1045.52 eV, shifting by 0.23 eV in the direction of low binding energy. Fig. 7b shows the 2p XPS plots of Co before and after boron doping, and it can be found that the characteristic peak binding energies of the $2p_{3/2}$ and $2p_{1/2}$ peaks of Co^{2+} are changed from 781.41 eV and 797.68 eV to 781.81 eV and 798.08 eV, respectively, and are shifted by 0.4 eV towards the direction of high binding energy. The XPS fitting results indicate that the introduction of boron causes the flow of electrons from CoS_2 to ZnS inside the heterojunction. This enhances the reduction of the negatively charged polysulfide anions due to the gain of electrons by ZnS, and enhances the adsorption of polysulfides due to the loss of electrons by CoS_2, which is positively charged. The results indicate that the uniform doping of boron can effectively modulate the electronic properties of the ZnS/CoS_2 heterostructures, thus exhibiting enhanced catalytic activity. Fig. 7c shows the S 2p XPS spectra of the B–ZnS/CoS_2@CS catalyst, in which the four sets of spin-split peaks, 161.94/163 eV; 163.02/164.04 eV; 164.08/165.29 eV and 168.95/170.02 eV, represent the S–S, M–S, C–S–C, and SO_4^{2-}, respectively.[50–52] The presence of the C–S–C bonds indicates that the catalyst is stretcher-loaded onto the carbon shell in the form of bonding, and this structural advantage lies in the ability of the carbon substrate to provide the catalyst with a strong electron transporting capability. The XPS spectrum of B 1s is shown in Fig. 7d, which displays a distinct characteristic peak at 187.56 eV. This is due to the generation of metal–boron bonding as a result of the doping of boron into the catalyst, suggesting a successful doping of boron.[53]

The adsorption capacity of the catalytic materials for LiPSs determines the utilization of the active substance, for which visual adsorption experiments were performed on the catalysts.

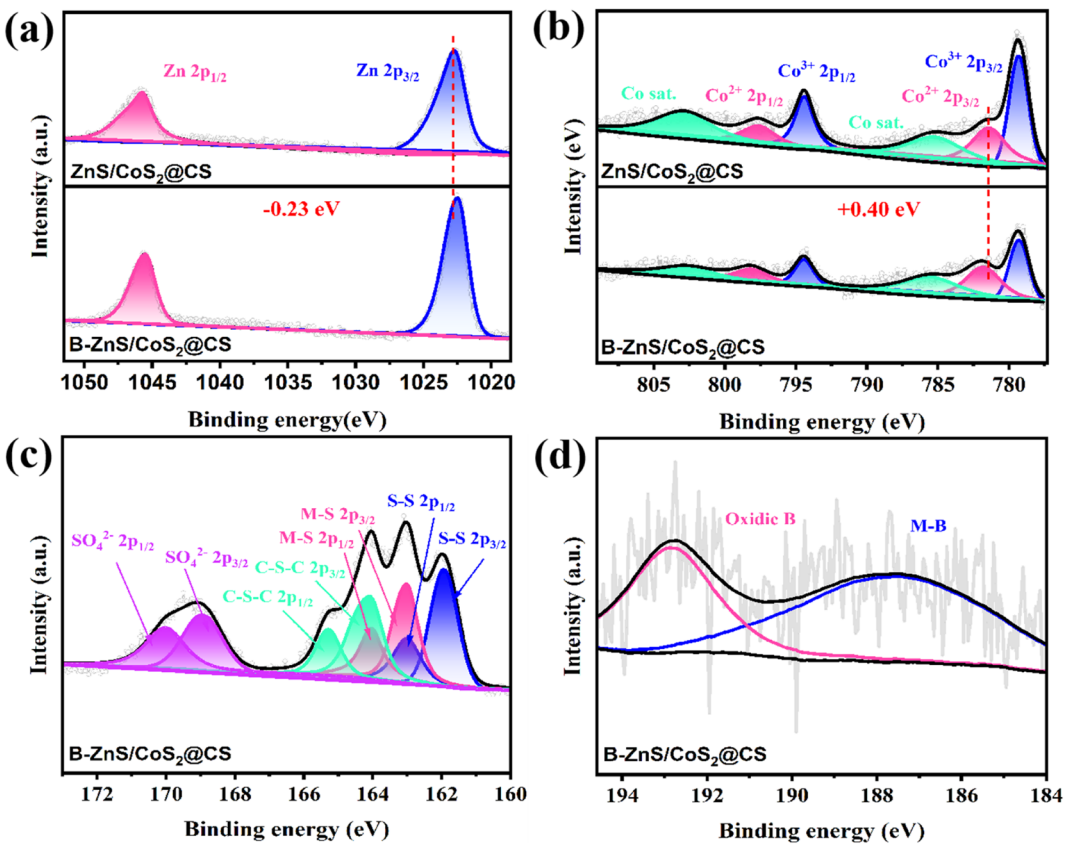

Fig. 7 (a) Zn 2p, (b) Co 2p, (c) S 2p and (d) B 1s XPS spectra of the ZnS/CoS_2@CS and B–ZnS/CoS_2@CS catalysts.

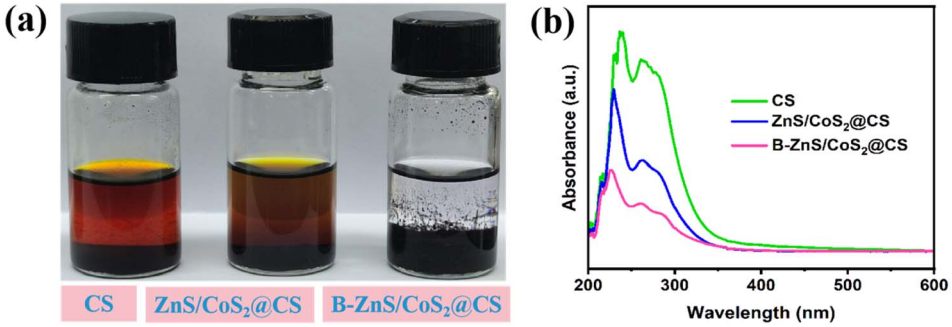

Fig. 8 (a) Digital photographs and (b) UV-vis spectra of different catalysts after soaking in Li_2S_6.

As shown in Fig. 8a, 100 mg of CS, ZnS/CoS_2@CS and B–ZnS/CoS_2@CS catalytic materials were placed in transparent glass vials, respectively, and 10 ml of 0.05 M Li_2S_6 solution was added to the interior and left to stand for 12 h. It was observed that the LiPSs solution impregnated with the B–ZnS/CoS_2@CS material became almost colorless. Conversely, the LiPSs solution impregnated with the CS- and the ZnS/CoS_2@CS materials still exhibited varying degrees of yellow color, although the LiPS solution with ZnS/CoS_2@CS was lighter in color compared to CS. The observed results indicated that the boron-doped catalyst could effectively improve the adsorption capacity of ZnS/CoS_2@CS on LiPSs. Meanwhile, it was found that the degree of adsorption capacity enhancement was less desirable after the ZnS/CoS_2 heterojunction catalysts were stretched on CS. This was due to the fact that the agglomerated morphology of the ZnS/CoS_2@CS catalysts affected the chemical adsorption strength of LiPSs to a certain extent. After the adsorption experiments, the supernatant was aspirated and diluted 100-fold with DOL/DME solvent mixture for ultraviolet-visible spectroscopy (UV-vis) testing. As shown in Fig. 8b, the UV-vis results agreed with the adsorption experimental observations. The solution impregnated with CS showed the highest Li_2S_6 peak intensity, the solution impregnated with ZnS/CoS_2@CS exhibited a slightly lower peak intensity, and the solution impregnated with B–ZnS/CoS_2@CS solution showed the lowest peak intensity, indicating that the boron-doped heterojunction catalyst has the best LiPSs adsorption capacity.

The particulate samples after the adsorption experiments were dried and analyzed for their chemical states using XPS. As shown in Fig. 9a, the Zn 2p XPS spectrum showed a set of characteristic peaks at 1022.30 eV and 1045.32 eV. These peaks were shifted by 0.2 eV towards low binding energy compared to that before adsorption, which was typical of Lewis acid–base interactions. The Co 2p XPS spectrum is shown in Fig. 9b, and the intensity of the characteristic peaks belonging to Co^{3+} was significantly reduced. From calculations, it was found that the

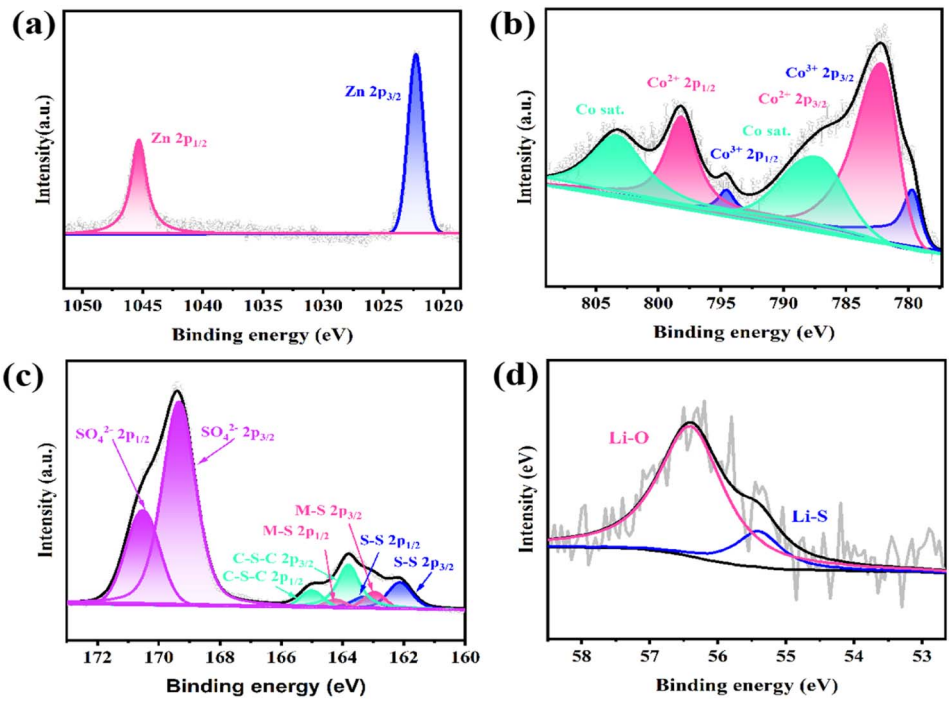

Fig. 9 XPS spectra of B–ZnS/CoS_2@CS after Li_2S_6 adsorption: (a) Zn 2p, (b) Co 2p, (c) S 2p and (d) Li 1s.

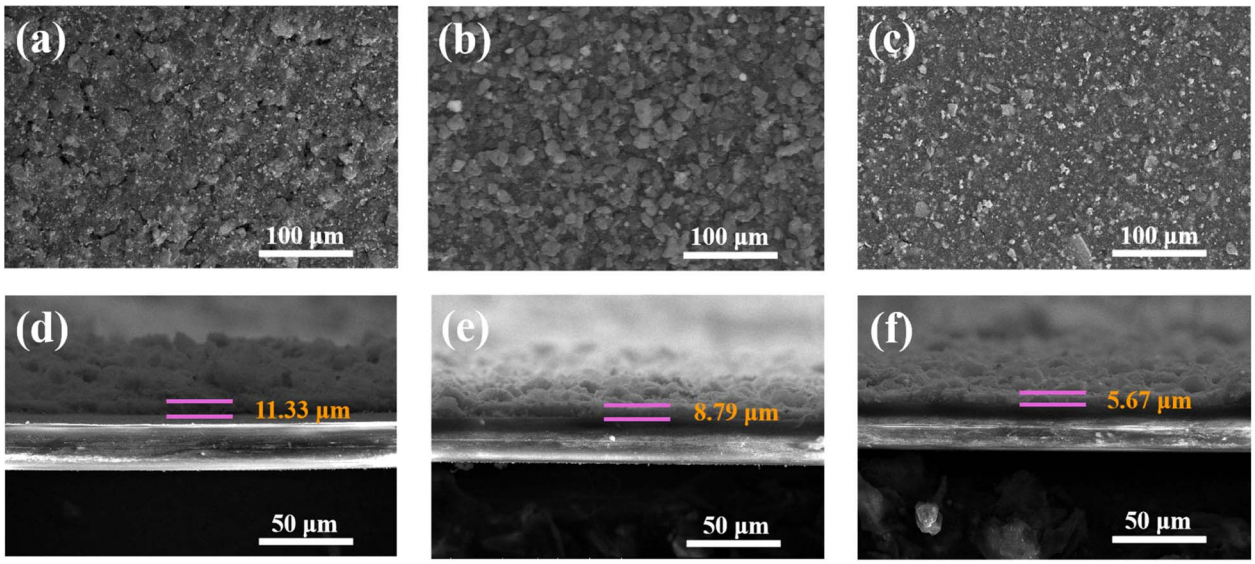

Fig. 10 Top SEM images of (a–c) CS, ZnS/CoS_2@CS and B–ZnS/CoS_2@CS-modified separators. Cross-sectional SEM images of (d–f) CS, ZnS/CoS_2@CS and B–ZnS/CoS_2@CS-modified separators.

percentage of Co^{3+} chemical state orbitals decreased from 28.1% to 11.1% before and after adsorption. Meanwhile, the characteristic peak of SO_4^{2-} shown in Fig. 9c belongs to the polysulfate complex. The increase of its peak intensity indicates the enhancement of oxidative strength from the side, which corresponds to the decrease of Co^{3+}.[54] Notably, the Li 1s XPS spectra (Fig. 9d) showed two characteristic peaks at 55.4 eV and 56.4 eV, corresponding to Li–S and Li–O bonds, respectively.[55,56] This suggests that the Li in the polysulfides is capable of strong chemical bonding with the B–ZnS/CoS_2@CS.

3.2 Analysis of the B–ZnS/CoS_2@CS modified septa

The CS, ZnS/CoS_2@CS and B–ZnS/CoS_2@CS catalysts with the same loading (0.4 mg cm^{-2}) were separately coated onto commercial Celgard membranes by vacuum filtration, and the morphology of the modified diaphragms is shown in Fig. 10a–c. The surfaces of the ZnS/CoS_2@CS and B–ZnS/CoS_2@CS modified membranes are relatively flat and uniform. The CS-modified film has slight cracks on the surface, which may lead to the uneven diffusion of ions. In turn, this may result in the uneven deposition of the passivation layer (Li_2S), formation of galvanic segregation, and "dead sulfur" during the cycling process after the assembly of the cell. The cross-sectional morphology of the different catalyst-modified films is shown in Fig. 10d–f. The coating thickness of B–ZnS/CoS_2@CS (Fig. 10f) is about 5.67 μm, and that of ZnS/CoS_2@CS (Fig. 10e) is about 8.79 μm, resulting from the agglomeration of the ZnS/CoS_2@CS catalyst. It was found through the SEM image of Fig. 2a that the carbon sheet material (CS) was the thickest coating layer (Fig. 10d) due to its light weight, which resulted in a coating layer of about 11.33 μm. The thinnest coating of the B–ZnS/CoS_2@CS catalysts will help to shorten the Li^+ diffusion path, which is the basis for ensuring the fast SRR and SER processes of LSBs.

Electrolyte contact angle tests of different catalyst-modified diaphragms (Fig. 11a–c) revealed that the contact angle of the B–ZnS/CoS_2@CS modified membrane (7.93°) was smaller than that of ZnS/CoS_2@CS (9.28°) and CS (17.26°). The results indicate that the B–ZnS/CoS_2@CS catalyst has the strongest ability to infiltrate the electrolyte, and the boron doping can increase the surface polarity of the catalyst and promote off-permeation.

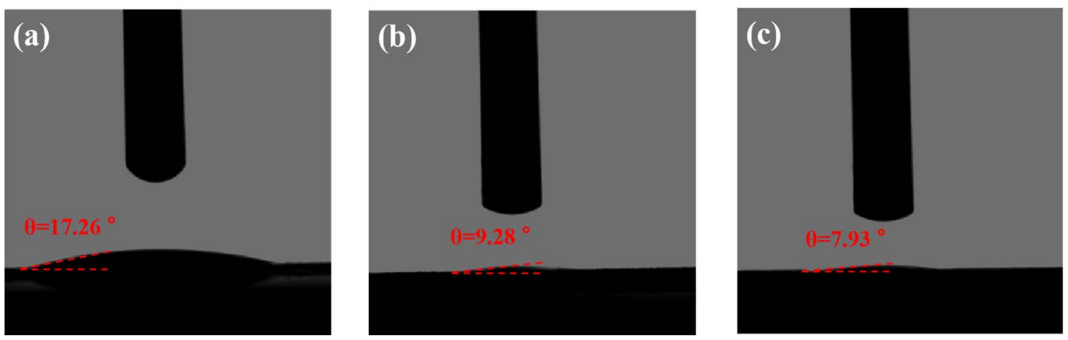

Fig. 11 The electrolyte contact angles of different separators: (a) CS, (b) ZnS/CoS_2@CS, and (c) B–ZnS/CoS_2@CS.

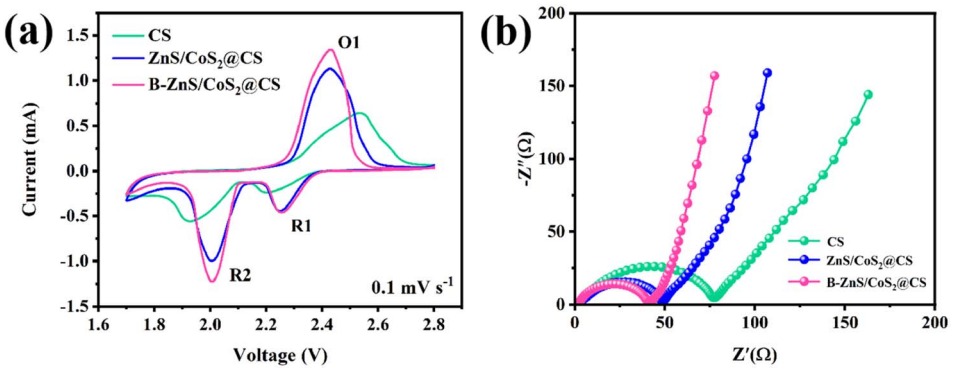

Fig. 12 (a) CV curves and (b) AC impedance spectra of LSBs assembled by the CS, ZnS/CoS_2@CS and B–ZnS/CoS_2@CS catalyst-modified separators.

3.3 Electrochemical performance analysis of B–ZnS/CoS_2@CS

Lithium–sulfur batteries were separately assembled using CS, ZnS/CoS_2@CS and B–ZnS/CoS_2@CS modified diaphragms, and subjected to cyclic voltammetry tests. As shown in Fig. 12a, the different cells all showed two obvious reduction peaks (R1 and R2) and one oxidation peak (O1), involving the reaction processes of the transformation of the solid-phase S_8 to liquid-phase long-chained LiPSs to insoluble Li_2S_2 and Li_2S, and the oxidation of Li_2S_2 and Li_2S to S_8, respectively. Compared with the CS and ZnS/CoS_2@CS cells, the B–ZnS/CoS_2@CS cell shows the largest peak current, indicating a significant kinetic advantage in SRR and SER. In addition, as shown by the EIS results (Fig. 12b), the CS, ZnS/CoS_2@CS and the charge of B–ZnS/CoS_2@CS transfer resistance of the battery is respectively 73.7 Ω, 44.1 Ω, and 37.8 Ω, indicating that the B–ZnS/CoS_2@CS cell has the smallest resistance between the electrode and electrolyte.

The cyclic voltammetry curves of LSBs with catalyst-modified diaphragms at 0.1–0.4 mV s^{-1} sweep rates are shown in Fig. 13a–c. As can be seen from the figure, the cell assembled with the B–ZnS/CoS_2@CS modified membrane has the largest peak response current compared to the ZnS/CoS_2@CS and CS cells, indicating that the B–ZnS/CoS_2@CS catalyst has the strongest redox catalytic effect on LiPSs. Moreover, the R1, R2 and O1 peaks were accompanied by an increase in the sweep rate, an increase in the polarization voltage, and a more pronounced shift in the linear increase of the peak current, suggesting that the redox kinetics of LiPSs during charging and discharging of LSBs were mainly affected by ion diffusion. Therefore, it is usually believed that the diffusion ability of Li^+ affects the conversion process of LiPSs, which in turn has a certain degree of influence on the performance of LSBs.

The diffusion behavior of Li^+ was investigated by CV curves with different sweep speeds. The B–ZnS/CoS_2@CS catalyst has the strongest ability to promote the diffusion of Li^+. This is

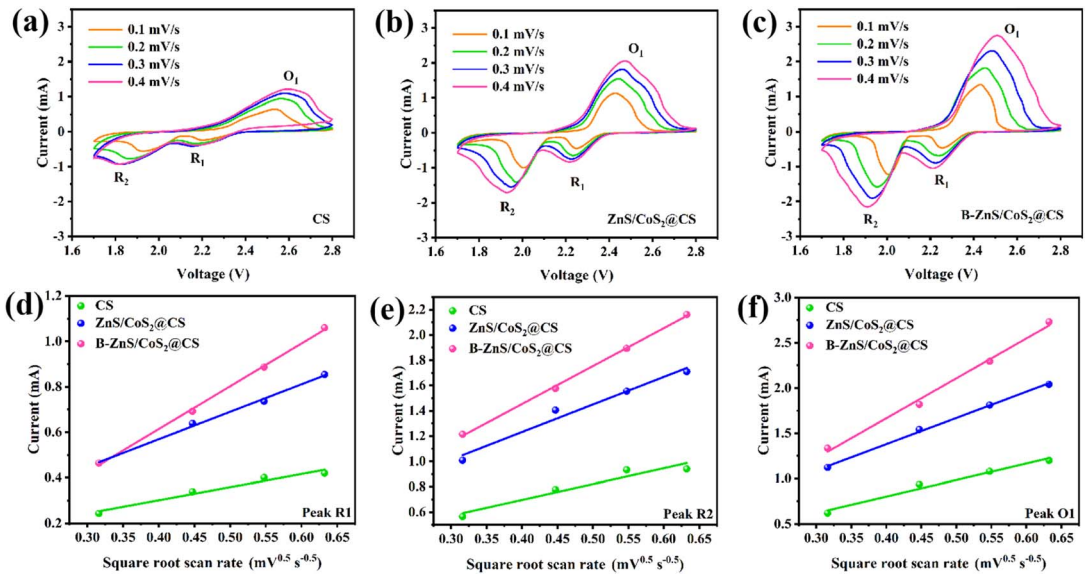

Fig. 13 (a) CV curves of LSBs assembled by CS, (b) ZnS/CoS_2@CS and (c) B–ZnS/CoS_2@CS catalyst-modified separators at different scan rates, and the relationship between the peak current and square root of the scan rate: (d) R1 peak, (e) R2 peak, and (f) O1 peak.

Table 1 D_{Li^+} and the related parameters for the R1, R2 and O1 peaks

	Peak	n	Slope of $I_p \times v^{-0.5}$	$D_{Li^+} \times 10^{10}$ cm^2 s^{-1}
CS	R1	0.5	−0.57	0.28
	R2	1.5	−1.25	0.05
	O1	2	−1.82	0.04
ZnS/CoS_2@CS	R1	0.5	−1.21	1.27
	R2	1.5	−2.18	0.16
	O1	2	−2.90	0.11
B–ZnS/CoS_2@CS	R1	0.5	−1.88	3.00
	R2	1.5	−3.00	0.29
	O1	2	−4.41	0.26

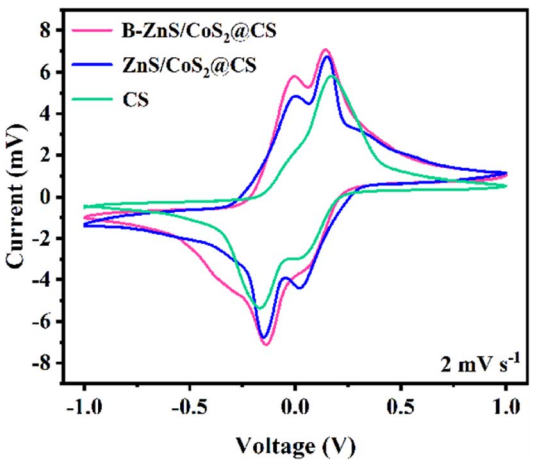

Fig. 14 CV of symmetric cells assembled by CS, ZnS/CoS_2@CS and B–ZnS/CoS_2@CS.

mainly due to the uniformly doped electron-deficient boron enhancing the Lewis acid nature of the ZnS/CoS_2@CS heterojunction, which in turn enhances the ability to inhibit the diffusion of the anions of LiPSs with extra lone-pair electrons. Based on the law of charge conservation, this will effectively accelerate the diffusion of lithium ions into the cathode of lithium ions to the anode.

The Li^+ diffusion coefficient (D_{Li^+}) can be calculated based on the slope of $I_p \times v^{-0.5}$. The values for different electrochemical reaction processes are shown in Table 1, and the D_{Li^+} values of the cells assembled with B–ZnS/CoS_2@CS modified membranes were 3.00×10^{-10}, 0.29×10^{-10}, and 0.26×10^{-10} cm^2 s^{-1} for the R1, R1, and O1 processes, respectively. These values were higher than those of the CS and ZnS/CoS_2@CS catalysts, indicating that the B–ZnS/CoS_2@CS catalyst has the strongest ability to promote Li^+ diffusion. The reason is the uniformly doped electron-deficient boron enhancing the Lewis acid nature of the ZnS/CoS_2@CS heterojunction, which in turn enhances the ability to inhibit the diffusion of LiPSs anions with extra lone-pair electrons, which, based on the law of charge conservation, will effectively accelerate the diffusion of lithium ions to the cathode.

Symmetric cells were assembled using different catalyst electrodes for CV and EIS tests. The CV curves at a sweep rate of 2 mV s^{-1} are shown in Fig. 14, where the CS symmetric cell shows the lowest response peak current and the largest polarization voltage. Meanwhile, the B–ZnS/CoS_2@CS symmetric cell exhibits a larger peak current and smaller polarization voltage than the ZnS/CoS_2@CS cell.

The conversion kinetics of LiPSs on the anodes of different catalysts was further investigated by linear scanning voltammetry (LSV). As shown in Fig. 15a, the peak response currents (absolute values) of the LSV curves for B–ZnS/CoS_2@CS, ZnS/CoS_2@CS, and CS were 9.723, 8.212, and 5.411 mA, respectively. This indicated that the catalytic ability of the B–ZnS/CoS_2@CS catalysts for the transition process of the soluble, long-chained LiPSs to the solid-phase Li_2S_2/Li_2S phase was stronger. The fitted Tafel curves (Fig. 15b) showed that the Tafel slopes of the B–ZnS/CoS_2@CS, ZnS/CoS_2@CS and CS are 0.538, 0.617 and 0.769 V dec^{-1}, respectively. The B–ZnS/CoS_2@CS electrodes had the smallest Tafel slopes, which indicated that they had the strongest reaction kinetics. The above results indicate that the boron-doped heterostructure contributes to the accelerated conversion kinetics of LiPSs.

The above results indicate that the B–ZnS/CoS_2@CS catalyst has the strongest kinetic promotion of LiPSs, which is further demonstrated by the Li_2S nucleation pattern of the catalyst cell.

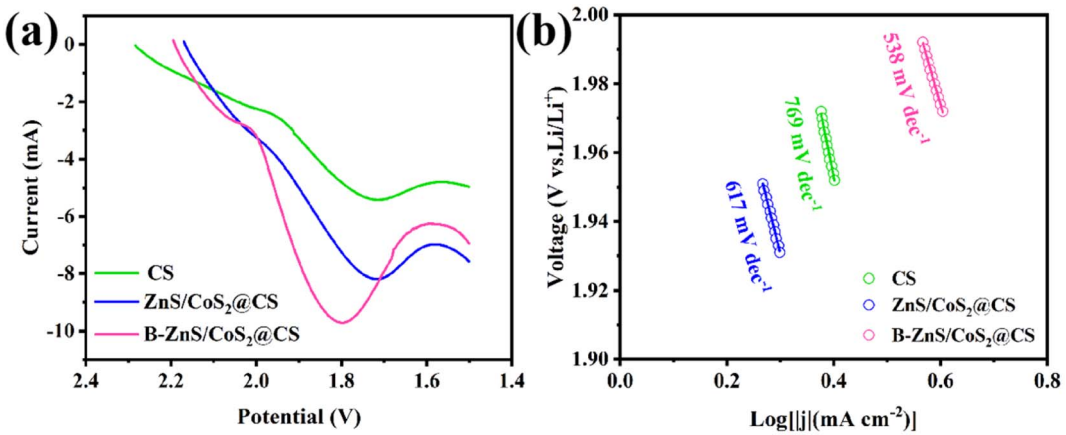

Fig. 15 (a) The LSV curves and (b) the corresponding Tafel curves of CS, ZnS/CoS_2@CS and B–ZnS/CoS_2@CS.

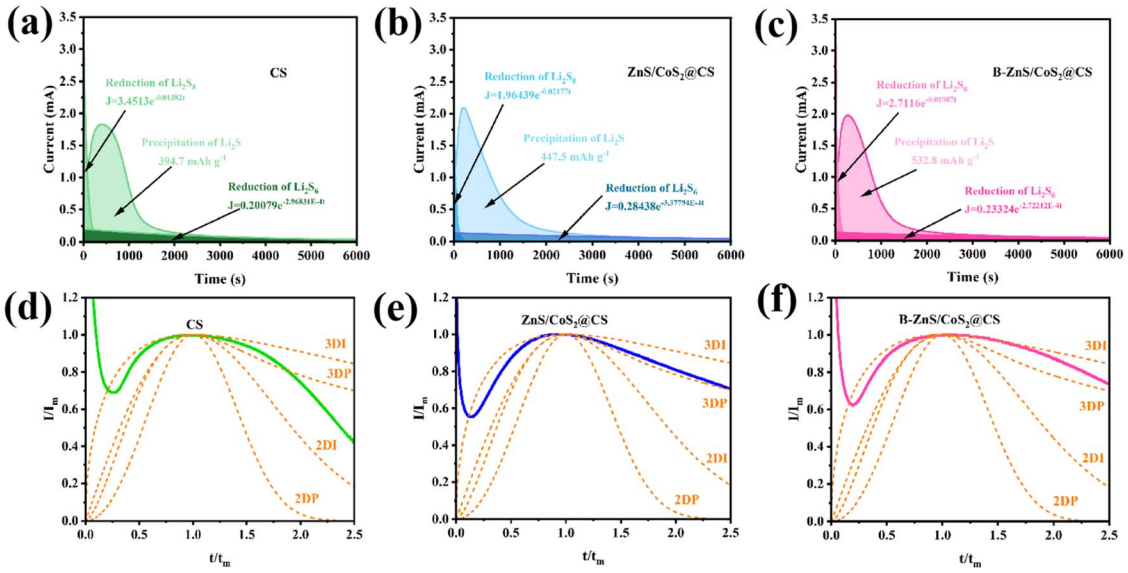

Fig. 16 Potentiostatic discharge curves of the Li_2S_8 electrolyte at 2.05 V on the (a) CS, (b) ZnS/CoS_2@CS, and (c) B–ZnS/CoS_2@CS cathodes, and dimensionless *i*–*t* transient fitting results of the Li_2S nucleation process on the (d) CS, (e) ZnS/CoS_2@CS and (f) B–ZnS/CoS_2@CS catalysts.

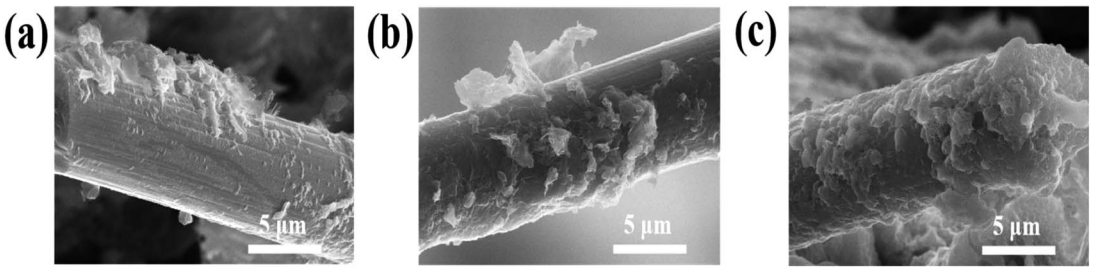

Fig. 17 SEM images of the Li_2S deposition on different catalyst electrodes: (a) CS; (b) ZnS/CoS_2@CS and (c) B–ZnS/CoS_2@CS.

As shown in Fig. 16a–c, comparing the nucleation process of Li_2S on the B–ZnS/CoS_2@CS, ZnS/CoS_2@CS and CS cathodes, it was found that its specific capacity contribution on B–ZnS/CoS_2@CS (532.8 mA h g^{-1}) was higher than that on ZnS/CoS2@CS (447.5 mA h g^{-1}) and CS (394.7 mA h g^{-1}), indicating that the B–ZnS/CoS_2@CS material has superior catalytic ability for Li_2S nucleation. The dimensionless analysis of the *i*–*t* curves based on the Li_2S nucleation process is shown in Fig. 16d–f. It can be observed that the Li_2S nucleation on the CS electrode is mainly dominated by two-dimensional instantaneous (2DI) and three-dimensional progressive (3DP) diffusion. Meanwhile, the modeling of the Li_2S nucleation on both ZnS/CoS_2@CS and B–ZnS/CoS_2@CS electrodes exhibits three-dimensional progressive (3DP) and three-dimensional instantaneous (3DI) mixed diffusion models, in which the electrodes of the boron-doped catalysts have some degree of improvement on the Li_2S nucleation.

Next, the Li_2S growth on the surfaces of different electrodes under the same test conditions was characterized by SEM. It was found that only a small amount of Li_2S was deposited on the CS electrode (Fig. 17a). Conversely, the Li_2S deposited on the ZnS/CoS_2@CS electrode (Fig. 17b) was significantly increased, but still not as much as that on the B–ZnS/CoS_2@CS electrode (Fig. 17c). The dense and uniform Li_2S grown on the surface may be due to the doping of boron, which exposes more nucleation sites in the heterostructure. The above results indicate that the B–ZnS/CoS_2@CS catalyst can effectively promote the transition kinetics of the liquid–solid phase and the uniform growth of Li_2S. This ensures the uniform charge transfer for the subsequent reaction, and then activates the oxidation of Li_2S and enhances the utilization of the active substance.

3.4 Battery performance based on the B–ZnS/CoS_2@CS modified diaphragm

The CS, ZnS/CoS_2@CS and B–ZnS/CoS_2@CS catalysts have been analyzed to understand how they play different degrees of catalytic roles in the SRR and SER kinetics of LiPSs, as well as Li_2S nucleation. The application capability of the catalyst-modified diaphragms was further investigated by different cell performance tests. Firstly, the constant-current intermittent titration test was conducted at 0.1C current on LSBs with different modified diaphragms, aiming to analyze the resistance changes inside different cells. As shown below, the B–ZnS/

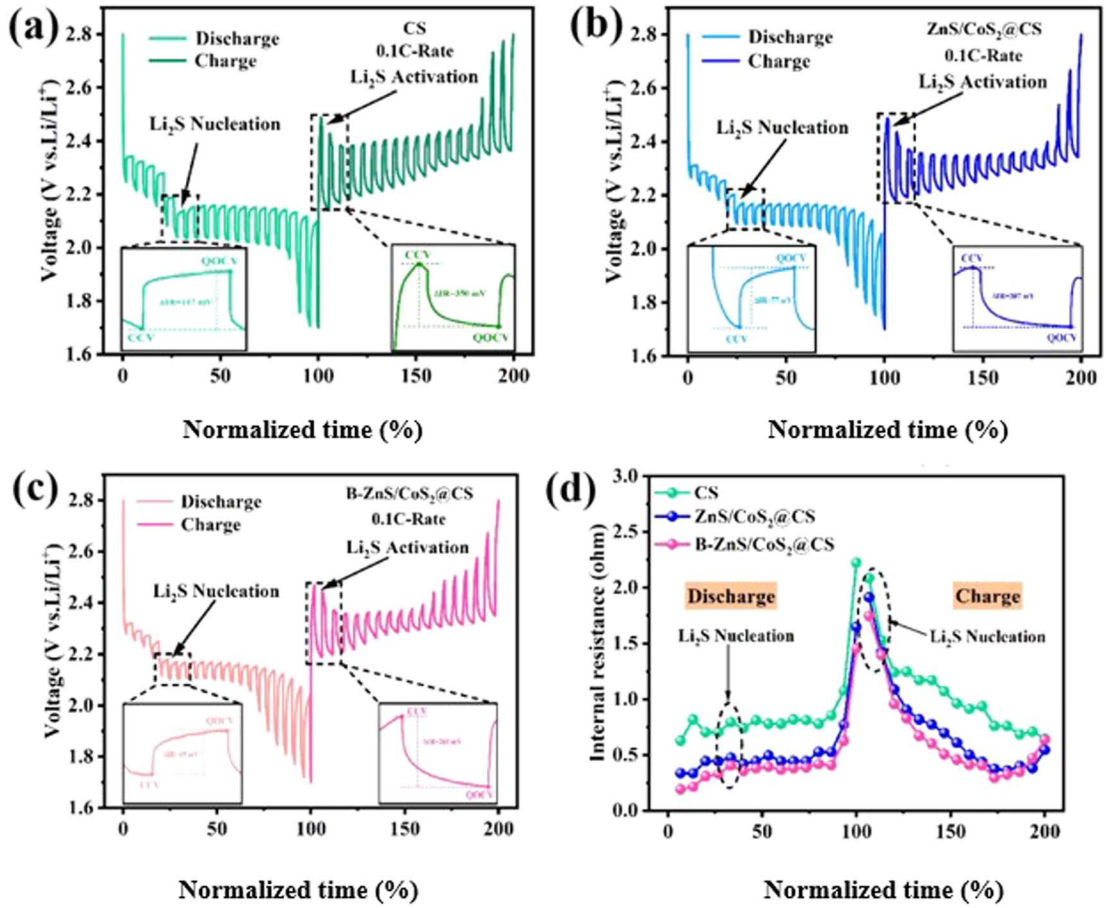

Fig. 18 GITT curves of (a) CS, (b) ZnS/CoS_2@CS, (c) B–ZnS/CoS_2@CS batteries, and (d) the internal resistance of different batteries based on the normalized discharge/charge time.

CoS_2@CS (Fig. 18c) modified membrane cell possesses a smaller polarization internal resistance than the CS (*e.g.*, Fig. 18a) and ZnS/CoS_2@CS (Fig. 18b) cells in the discharge/charge curves. In particular, during the Li_2S nucleation and dissolution process corresponding to the LSBs decisive step, the ΔiR of the B–ZnS/CoS_2@CS modified membrane cells were 65 and 269 mV, respectively. Meanwhile, the ΔiR of the ZnS/CoS_2@CS cells were 77 and 307 mV, respectively, and that of the CS cells were 117 and 350 mV, respectively. This indicated that the B–ZnS/CoS_2@CS catalysts promote the mass transfer of lithium and polysulfide ions inside the cell the most, and can effectively reduce the reaction energy barrier of the solid–liquid phase transition. The real-time internal resistance change (ΔR) of the cell during the testing process is presented by calculation in Fig. 18d. It can be observed that the internal resistance of the B–ZnS/CoS_2@CS cell is significantly smaller than that of the ZnS/CoS_2@CS and CS cells. This may be attributed to the fact that the B–ZnS/CoS_2@CS catalyst combines the advantages of the conductive network CS and the electron-deficient boron for the modulation of electron transport ability, while the further enhanced Lewis acid nature on the ZnS/CoS_2 heterostructure accelerates the mass transfer of LiPSs.

LSBs button batteries were assembled using different catalytic materials modified diaphragms, and their performance was tested and analyzed. The battery multiplicity performance is shown in Fig. 19a, from which it can be seen that the specific capacity of discharge at adopting B–ZnS/CoS_2@CS are 0.2, 0.5, 1, 2, 3, 4, 5 and 6C multiplicities are 1241.5, 1058.5, 954.2, 861.9, 732.1, 610.8, 495.6 and 370.7 mA h g^{-1}, respectively. The specific capacity also almost returned to the initial state when the cell recovered to 0.5C and 0.2C. Compared with the B–ZnS/CoS_2@CS catalyst-modified diaphragm, the LSBs with ZnS/CoS_2@CS and CS-modified membranes provided a lower discharge specific capacity, especially at 6C. The ZnS/CoS_2@CS and CS batteries can only contribute 136.9 and 50 mA h g^{-1} specific capacity, respectively. The results indicate that the boron-doped heterostructured catalysts have a significant effect on the improvement of the battery performance.

The first turn constant-current charge/discharge curves of CS, ZnS/CoS_2@CS and B–ZnS/CoS_2@CS at 2C are shown in Fig. 19b. It can be observed that the LSBs cell with the B–ZnS/CoS_2@CS diaphragm has the smallest polarization voltage, and the smallest charging/discharging overpotential during Li_2S nucleation and dissolution. It is noteworthy that ZnS/CoS_2@CS shows no significant improvement in polarization relative to CS,

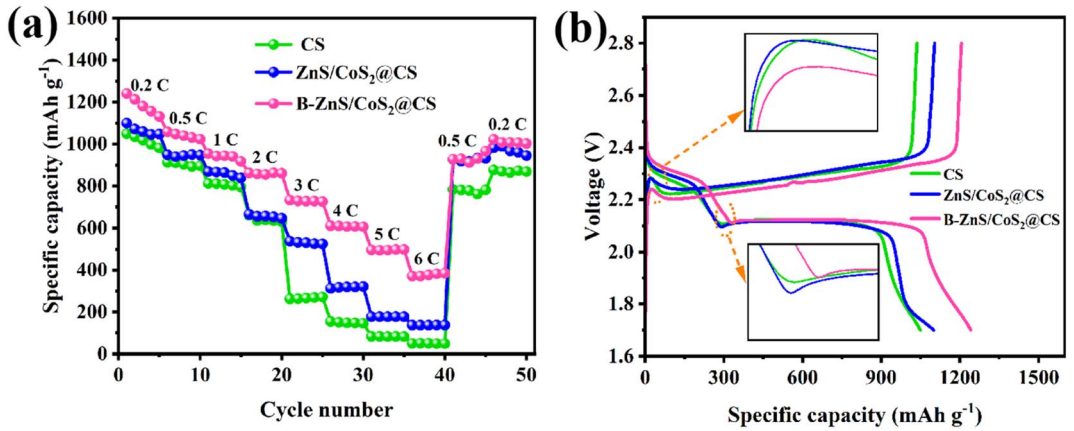

Fig. 19 Rate performance of batteries assembled with different separators: (a) rate performance and (b) charge/discharge curve of the 0.2C first cycle.

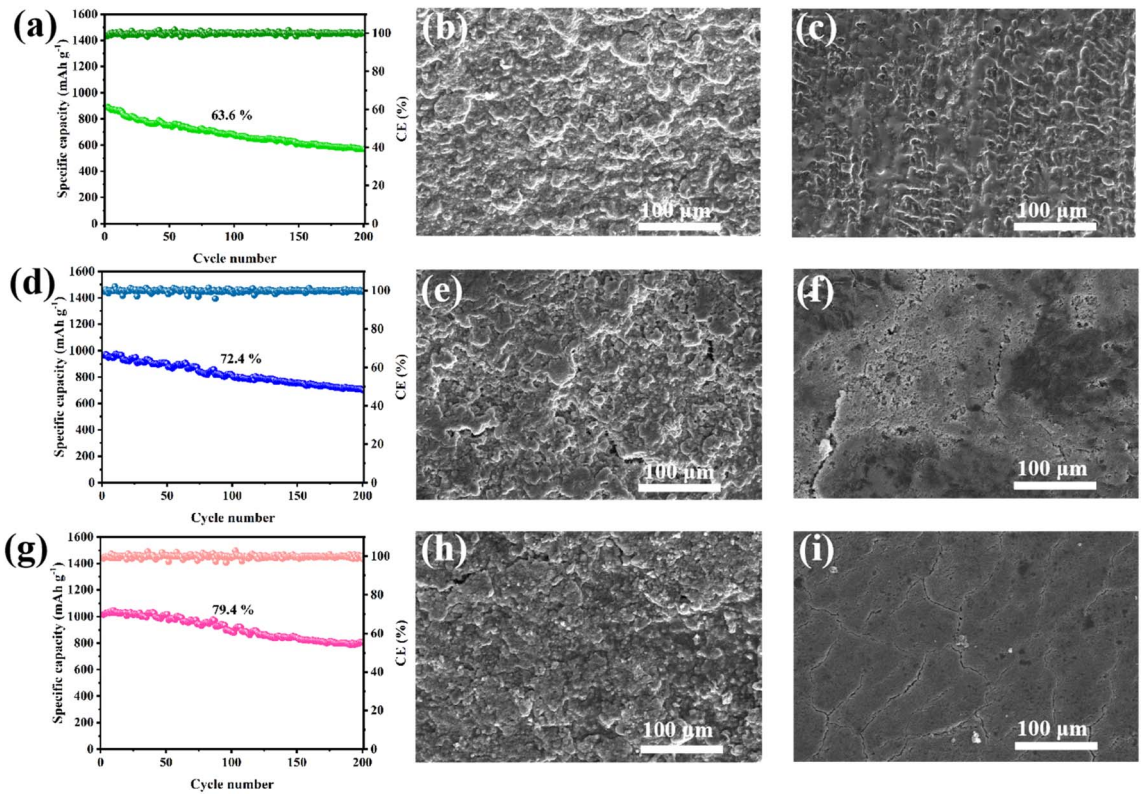

Fig. 20 0.5C cycle performance and SEM images of separators and lithium plates after cycling: (a) CS, (d) ZnS/CoS_2@CS, and (g) B–ZnS/CoS_2@CS, corresponding to (b, e and h) separators and (c, f and i) lithium plates after cycling.

and presents a larger charging/discharging overpotential on the constant-current charging/discharging curves. This may be attributed to the agglomeration of the ZnS/CoS_2 heterojunction catalysts loaded on CS, resulting in a larger electron transfer energy barrier during the reduction–oxidation reaction of Li_2S.

LSBs with different catalyst-modified diaphragms were subjected to a 0.5C short cycle test, and the results are shown in Fig. 20. The initial specific capacities of LSBs assembled with B–ZnS/CoS_2@CS, ZnS/CoS_2@CS, and CS catalyst-modified diaphragms were 1016 mA h g^{-1}, 965.8 mA h g^{-1}, and 893.6 mA h g^{-1}, respectively. After 200 charging and discharging cycles, the specific capacities decreased to 806.2 mA h g^{-1}, 698.6 mA h g^{-1} and 567.9 mA h g^{-1}, respectively. Furthermore, the capacity retention of the batteries assembled with different modified membranes were calculated to be 79.4%, 72.4% and 63.6% for B–ZnS/CoS_2@CS, ZnS/CoS_2@CS, and CS catalyst-modified membranes, respectively. The results show that the B–ZnS/CoS_2@CS catalyst-modified membranes can effectively

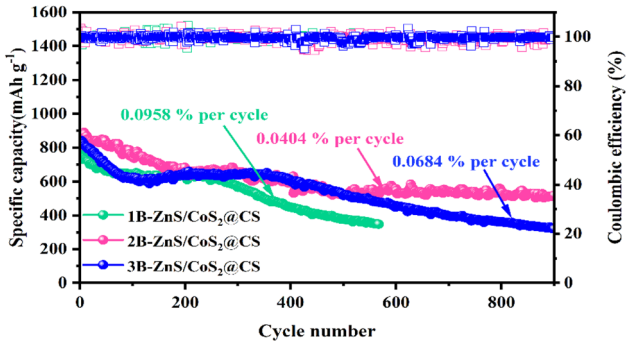

Fig. 21 Comparison of the cycle performance of the B–ZnS/CoS_2@CS catalyst batteries with different boron doping amounts at 1.0C.

improve the cycling stability of LSBs. The surface morphology of the post-cycling diaphragms was observed by SEM. It was found that the surface of the post-cycling CS-modified membranes (Fig. 20b) showed many inhomogeneous Li_2S_2/Li_2S passivation layers. Conversely, the passivation layers on the surfaces of the ZnS/CoS_2@CS (Fig. 20e) and B–ZnS/CoS_2@CS (Fig. 20h)-modified membranes exhibited a thinner and more homogeneous deposition. Even in the case of the B–ZnS/CoS_2@CS modified film, the surface can also be observed with obvious catalytic materials, indicating that the boron-doped catalyst can effectively enhance the utilization of sulfur as the active substance by the heterojunction. In addition, by observing the surface of the lithium wafers after different cell cycles, the growth of lithium dendrites was found to be significantly different. Among them, dense lithium dendrites were distributed on the surface of lithium wafers of LSBs assembled with CS-modified film (Fig. 20c). The lithium dendrite growth on the surface of the lithium wafers of the battery with ZnS/CoS_2@CS-modified film was improved to a great extent (Fig. 20f). Only a small amount of dendritic crystal growth existed in localized areas. In the battery with boron-doped catalysts, there was hardly any obvious dendritic crystals observed on the surface of the lithium wafers (Fig. 20i). This indicated that the B–ZnS/CoS_2@CS catalyst can effectively inhibit the growth of lithium dendrites.

Subsequently, B–ZnS/CoS_2@CS catalysts with different boron doping amounts were used to modify the diaphragm and assemble the cell, and the cycling performance was tested at 1.0C. As shown in Fig. 21, the 2B–ZnS/CoS_2@CS catalyst prepared with 5 mmol of boron-sourced dopant endowed the battery with the best long-cycle performance, with an initial specific capacity of 815.4 mA h g^{-1} for the LSBs. The specific capacity was maintained at 519.1 mA h g^{-1} after 900 cycles, with a retention rate of 63.66% and an average decay rate of 0.0404% per cycle, which is a good cycling performance. The average decay rate per cycle was 0.0648% for the 1B–ZnS/CoS_2@CS catalyst prepared by 1 mmol boron source dopant, causing the cell to exhibit the worst cycling specific capacity retention rate (45.7%) in a shorter cycle. Average decay rate per cycle is 0.0958%.

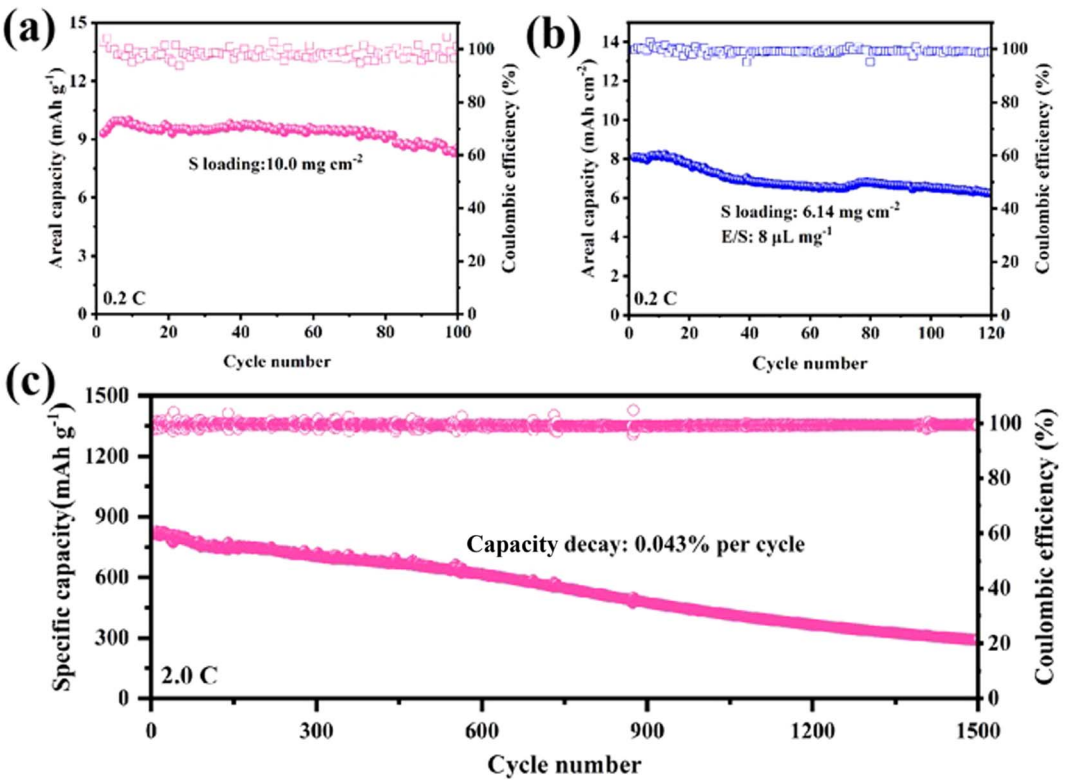

Fig. 22 The cycle performance of LSBs assembled with the B–ZnS/CoS_2@CS separator: (a) 10.0 mg cm^{-2} high sulfur loading cycle performance, (b) 6.14 mg cm^{-2} high sulfur loading cycle performance at low E/S ratio, and (c) 2.0C long-cycle performance.

3.5 The advantages of the B–ZnS/CoS_2@CS catalyst-modified diaphragms for LSBs were further analyzed by long-cycle tests under high sulfur loading conditions

As shown in Fig. 22a, the initial area-specific capacity of LSBs was 9.312 mA h cm^{-2} at 0.2C multiplicity at a sulfur content as high as 10.0 mg cm^{-2}. The specific capacity could still be maintained at 8.586 mA h cm^{-2} after 100 charge/discharge cycles, with a retention rate as high as 92.2%. Since the electrolyte is an inactive substance in LSBs, and excess electrolyte affects the energy density of LSBs, the performance of LSBs under depleted (liquid–sulfur ratio E/S of 8 μl mg^{-1}) and high sulfur-carrying (6.14 mg cm^{-2}) conditions was examined. It was found that the cell was able to maintain a high area-specific capacity of 6.224 mA h cm^{-2} after 120 cycles (Fig. 22b). Subsequently, the cycle life of LSBs with the B–ZnS/CoS_2@CS-modified film was tested, and the results are shown in Fig. 22c. The cell could provide a first-cycle specific capacity of 820.9 mA h g^{-1} at 2.0C multiplicity. After 1500 cycles, the specific capacity retained 288.6 mA h g^{-1} with an average decay rate of 0.043% per cycle, indicating that the use of the B–ZnS/CoS_2@CS catalyst-modified membrane LSBs still achieved stable battery performance even under the harsher conditions, which has a better application prospect.

4. Conclusion and outlook

The "shuttle effect" within lithium–sulfur batteries severely affects sulfur utilization, which in turn exhibits low coulombic efficiency and cycle life. Transition metal catalysts are often used as diaphragm modification materials to adsorb LiPSs due to their high polarity and electrocatalytic activity. However, the single catalytic site limits the improvement of the battery performance. To address this issue, boron doping strategies were adopted to modify sulfide heterojunctions, to enhance the adsorption and catalytic ability of the catalysts for LiPSs, and improve the sulfur utilization rate and cycle life of LSBs. The main conclusions are as follows: carbon substrate (CS) was prepared by pyrolysis of sodium citrate, and boron-doped ZnS/CoS_2 heterojunction catalysts were generated on CS by one-step hydrothermal method to be used for the diaphragm modification layer. The B–ZnS/CoS_2@CS catalysts retained CS morphology well, and the uniform introduction of the electron-deficient boron enabled the catalysts to show strong Lewis acid properties. In turn, this effectively inhibited the diffusion of LiPSs anions with extra lone-pair electrons. The modified diaphragm has excellent performance in terms of cell multiplication and cycling performance, providing a high specific capacity of 384.2 mA h g^{-1} at a high multiplication rate of 6.0C. After 1500 charge/discharge cycles at 2.0C, the average decay rate of the cell's specific capacity per turn is as low as 0.043%. With a high sulfur loading of 10.0 mg cm^{-2}, the area-specific capacity of the cell can still provide a high specific capacity of 384.2 mA h g^{-1} at 0.2C after 100 charge/discharge cycles. After 100 charge/discharge cycles at 0.2C under a high sulfur load of 10.0 mg cm^{-2}, the battery is still able to provide an area-specific capacity of 8.586 mA h cm^{-2}, with a capacity retention rate as high as 92.2%.

In this paper, the structures of bimetallic sulfides were modified by different boron doping strategies. The catalytic effect of the catalyst-modified diaphragms on the redox of polysulfides was further investigated, which suppressed the shuttle effect and achieved higher sulfur utilization to different extents, providing a certain reference value for the enhancement of metal compounds in the field of lithium–sulfur battery diaphragm catalysts for higher performance. However, the following shortcomings of this paper are still worth exploring in the future:

(1) The nucleation and dissolution kinetics of Li_2S have a crucial position in the field of lithium–sulfur battery catalysis. Investigating the role of catalysts in controlling the nucleation behavior of Li_2S through theoretical calculations and advanced *in situ* techniques will help to design more efficient catalytic materials.

(2) Heteroatoms and transition metal compounds belong to two major classes of systems. It is worth studying the various synergistic catalytic effects from the doping of heteroatoms (other than boron) and compounds (other than oxides and sulfides).

Data availability

Data will be made available on request.

Author contributions

Jiayi Ren: data curation, writing – original draft. Qihao Zhao: dara curation, experiment.

Conflicts of interest

The authors declare that they have no known competing financial interests or personal relationships that could have appeared to influence the work reported in this paper.

References

1 L. Li, D. Zhang, J. Deng, *et al.*, Carbon-based materials for fast charging lithium-ion batteries, *Carbon*, 2021, **183**, 721–734.
2 A. Fotouhi, D. J. Auger, K. Propp, *et al.*, A review on electric vehicle battery modelling: from lithium-ion toward lithium-sulphur, *Renewable Sustainable Energy Rev.*, 2016, **56**, 1008–1021.
3 Y. Chen, T. Wang, H. Tian, *et al.*, Advances in Lithium-Sulfur Batteries: From Academic Research to Commercial Viability, *Adv. Mater.*, 2021, **33**(29), 2003666.
4 A. Eftekhari and D.-W. Kim, Cathode materials for lithium-sulfur batteries: a practical perspective, *J. Mater. Chem. A*, 2017, **5**(34), 17734–17776.
5 K. Zhang, Z. Chen, R. Ning, *et al.*, Single-Atom Coated Separator for Robust Lithium-Sulfur Batteries, *ACS Appl. Mater. Interfaces*, 2019, **11**(28), 25147–25154.

6 H. Zhao, N. Deng, J. Yan, *et al.*, A review on anode for lithium-sulfur batteries: progress and prospects, *Chem. Eng. J.*, 2018, **347**, 343–365.

7 V. Venkatachalam, A. Alsalme, A. Alswieleh, *et al.*, Double hydroxide mediated synthesis of nanostructured $ZnCo_2O_4$ as high performance electrode material for supercapacitor applications, *Chem. Eng. J.*, 2017, **321**, 474–483.

8 Y. Zhang, P. Chen, Q. Wang, *et al.*, High-Capacity and Kinetically Accelerated Lithium Storage in MoO_3 Enabled by Oxygen Vacancies and Heterostructure, *Adv. Energy Mater.*, 2021, **11**(31), 2101712.

9 J. Zhu, D. Song, T. Pu, *et al.*, Two-dimensional porous $ZnCo_2O_4$ thin sheets assembled by 3D nanoflake array with enhanced performance for aqueous asymmetric supercapacitor, *Chem. Eng. J.*, 2018, **336**, 679–689.

10 X. Chang, L. Zang, S. Liu, *et al.*, In situ construction of yolk-shell zinc cobaltite with uniform carbon doping for high performance asymmetric supercapacitors, *J. Mater. Chem. A*, 2018, **6**(19), 9109–9115.

11 S. Qiao, Q. Wang, D. Lei, *et al.*, Oxygen vacancy enabled fabrication of dual-atom Mn/Co catalysts for high-performance lithium-sulfur batteries, *J. Mater. Chem. A*, 2022, **10**(21), 11702–11711.

12 J. Lei, T. Liu, J. Chen, *et al.*, Exploring and Understanding the Roles of Li_2S_n and the Strategies to beyond Present Li-S Batteries, *Chem*, 2020, **6**(10), 2533–2557.

13 J. Wu, T. Ye, Y. Wang, *et al.*, Understanding the Catalytic Kinetics of Polysulfide Redox Reactions on Transition Metal Compounds in Li-S Batteries, *ACS Nano*, 2022, **16**(10), 15734–15759.

14 C. Zha, S. Wang, C. Liu, *et al.*, Single-atom tailoring of Li_2S to Form Li_2S_2 for building better lithium-sulfur batteries, *Energy Storage Mater.*, 2022, **47**, 79–86.

15 J. Wang, Y. Zhu, N. Wu, *et al.*, Designing thermotolerant and flame-resistant PAN-based separator via surface engineering with heteroatoms doped carbon framework encapsulated with CoS_2 nanocatalysts towards safe lithium-sulfur batteries, *Composites, Part B*, 2022, **233**, 109644.

16 B. Guo, Q. Ma, L. Zhang, *et al.*, Yolk-shell porous carbon spheres@$CoSe_2$ nanosheets as multilayer defenses system of polysulfide for advanced Li-S batteries, *Chem. Eng. J.*, 2021, **413**, 127521.

17 J. Liu, Z. Qiao, Q. Xie, *et al.*, Phosphorus-Doped Metal-Organic Framework-Derived CoS_2 Nanoboxes with Improved Adsorption-Catalysis Effect for Li-S Batteries, *ACS Appl. Mater. Interfaces*, 2021, **13**(13), 15226–15236.

18 W. Ahn, S. N. Lim, D. U. Lee, *et al.*, Interaction mechanism between a functionalized protective layer and dissolved polysulfide for extended cycle life of lithium sulfur batteries, *J. Mater. Chem. A*, 2015, **3**(18), 9461–9467.

19 Q. Sun, B. Xi, J.-Y. Li, *et al.*, Nitrogen-Doped Graphene-Supported Mixed Transition-Metal Oxide Porous Particles to Confine Polysulfides for Lithium-Sulfur Batteries, *Adv. Energy Mater.*, 2018, **8**(22), 1800595.

20 Y. Liu, Z. Ma, G. Yang, *et al.*, Multifunctional $ZnCo_2O_4$ Quantum Dots Encapsulated In Carbon Carrier for Anchoring/Catalyzing Polysulfides and Self-Repairing Lithium Metal Anode in Lithium-Sulfur Batteries, *Adv. Funct. Mater.*, 2021, **32**(12), 2109462.

21 B. Hu, J. Xu, Z. Fan, *et al.*, Covalent Organic Framework Based Lithium-Sulfur Batteries: Materials, Interfaces, and Solid-State Electrolytes, *Adv. Energy Mater.*, 2023, **13**(10), 2203540.

22 P. O. Schmidt, T. Rosenband, C. Langer, *et al.*, Spectroscopy using quantum logic, *Science*, 2005, **309**(5735), 749–752.

23 Q. Yang, X. Niu, Y. Zhu, *et al.*, Modulating anion defect in $La_{0.6}Sr_{0.4}Co_{0.8}Fe_{0.2}O_{3-\delta}$ for enhanced catalytic performance on peroxymonosulfate activation: Importance of hydrated electrons and metal-oxygen covalency, *J. Hazard. Mater.*, 2022, **432**, 128686.

24 S. Qiao, D. Lei, Q. Wang, *et al.*, Etch-evaporation enabled defect engineering to prepare high-loading Mn single atom catalyst for Li-S battery applications, *Chem. Eng. J.*, 2022, **442**, 136258.

25 L. Fan, N. Deng, J. Yan, *et al.*, The recent research status quo and the prospect of electrolytes for lithium sulfur batteries, *Chem. Eng. J.*, 2019, **369**, 874–897.

26 H. Yuan, W. Zhang, J.-g. Wang, *et al.*, Facilitation of sulfur evolution reaction by pyridinic nitrogen doped carbon nanoflakes for highly-stable lithium-sulfur batteries, *Energy Storage Mater.*, 2018, **10**, 1–9.

27 C. Y. Fan, Y. P. Zheng, X. H. Zhang, *et al.*, High-Performance and Low-Temperature Lithium-Sulfur Batteries: Synergism of Thermodynamic and Kinetic Regulation, *Adv. Energy Mater.*, 2018, **8**(18), 1703638.

28 J. Li, L. Gao, F. Pan, *et al.*, Engineering Strategies for Suppressing the Shuttle Effect in Lithium-Sulfur Batteries, *Nano-Micro Lett.*, 2023, **16**(1), 12.

29 D. M. Brieske, A. Warnecke and D. U. Sauer, Modeling the volumetric expansion of the lithium-sulfur battery considering charge and discharge profiles, *Energy Storage Mater.*, 2023, **55**, 289–300.

30 L. Hencz, Z. Wu, M. Zheng, *et al.*, Sustainable "Sweet and Salty" Synthesis of Hierarchical Porous Carbon for Lithium-Sulfur Batteries, *ACS Appl. Energy Mater.*, 2022, **5**(4), 4991–5001.

31 C.-C. Chuang, Y.-Y. Hsieh, W.-C. Chang, *et al.*, Phosphorus-sulfur/graphene composites as flexible lithium-sulfur battery cathodes with super high volumetric capacity, *Chem. Eng. J.*, 2020, **387**, 123904.

32 M. Zheng, X. Cai, Y. Tan, *et al.*, A high-resilience and conductive composite binder for lithium-sulfur batteries, *Chem. Eng. J.*, 2020, **389**, 124404.

33 J. Zou, P. He, Y. Zhang, *et al.*, An electrolyte additive of bromoxoindole enables uniform Li-ion flux and tunable Li_2S deposition for high-performance lithium-sulfur batteries, *J. Mater. Chem. A*, 2024, **12**(9), 5520–5529.

34 X. Liu, J. Q. Huang, Q. Zhang, *et al.*, Nanostructured Metal Oxides and Sulfides for Lithium-Sulfur Batteries, *Adv. Mater.*, 2017, **29**(20), 1601759.

35 S. Deng, T. Guo, J. Heier, *et al.*, Unraveling Polysulfide's Adsorption and Electrocatalytic Conversion on Metal Oxides for Li-S Batteries, *Adv. Sci.*, 2022, **10**(5), 2204930.

36 P. Chen, T. Wang, F. Tang, *et al.*, Elaborate interface design of CoS_2/Fe_7S_8/NG heterojunctions modified on a polypropylene separator for efficient lithium-sulfur batteries, *Chem. Eng. J.*, 2022, **446**, 136990.
37 P. Bonnick, K. Niitani, M. Nose, *et al.*, A high performance all solid state lithium sulfur battery with lithium thiophosphate solid electrolyte, *J. Mater. Chem. A*, 2019, **7**(42), 24173–24179.
38 Z. An, S. Xu, J. H. Lee, *et al.*, Crown ether complex-incorporated Li-ion selective separators for high-performance Li-S batteries, *Mater. Today Energy*, 2023, **36**, 101345.
39 Q. Zhang, X. Zhang, S. Qiao, *et al.*, Synthesis of the Ni_2P-Co Mott-Schottky Junction as an Electrocatalyst to Boost Sulfur Conversion Kinetics and Application in Separator Modification in Li-S Batteries, *ACS Appl. Mater. Interfaces*, 2023, **15**(4), 5253–5264.
40 R. Zhang, Y. Dong, M. A. Al-Tahan, *et al.*, Insights into the sandwich-like ultrathin Ni-doped MoS_2/rGO hybrid as effective sulfur hosts with excellent adsorption and electrocatalysis effects for lithium-sulfur batteries, *J. Energy Chem.*, 2021, **60**, 85–94.
41 B. Wang, L. Wang, B. Zhang, *et al.*, Niobium Diboride Nanoparticles Accelerating Polysulfide Conversion and Directing Li_2S Nucleation Enabled High Areal Capacity Lithium-Sulfur Batteries, *ACS Nano*, 2022, **16**(3), 4947–4960.
42 S. Qiao, Q. Wang, Q. Zhang, *et al.*, Sacrificial Template Method to Synthesize Atomically Dispersed Mn Atoms on S, N-Codoped Carbon as a Separator Modifier for Advanced Li-S Batteries, *ACS Appl. Mater. Interfaces*, 2022, **14**(37), 42123–42133.
43 Z. Li, Q. Zhang, L. Hencz, *et al.*, Multifunctional cation-vacancy-rich $ZnCo_2O_4$ polysulfide-blocking layer for ultrahigh-loading Li-S battery, *Nano Energy*, 2021, **89**, 106331.
44 W. Hou, P. Feng, X. Guo, *et al.*, Catalytic Mechanism of Oxygen Vacancies in Perovskite Oxides for Lithium-Sulfur Batteries, *Adv. Mater.*, 2022, **34**(26), e2202222.
45 J. Xu, J. Li, Y. Li, *et al.*, Long-Life Lithium-Metal All-Solid-State Batteries and Stable Li Plating Enabled by In Situ Formation of Li_3PS_4 in the SEI Layer, *Adv. Mater.*, 2022, **34**(34), e2203281.
46 Q. Wang, S. Qiao, Q. Zhang, *et al.*, Vacancy-rich, multi-heterostructured MXene/Fe_3S_4@$FeSe_2$ catalyst for high performance lithium-sulfur batteries, *Chem. Eng. J.*, 2023, **477**, 147100.
47 Q. Zhang, X. Zhang, D. Lei, *et al.*, MOF-Derived Hollow Carbon Supported Nickel-Cobalt Alloy Catalysts Driving Fast Polysulfide Conversion for Lithium-Sulfur Batteries, *ACS Appl. Mater. Interfaces*, 2023, **15**(12), 15377–15386.
48 L. Zhang, Y. Wang, Z. Niu, *et al.*, Advanced nanostructured carbon-based materials for rechargeable lithium-sulfur batteries, *Carbon*, 2019, **141**, 400–416.
49 C. Shi, J. Huang, Y. Tang, *et al.*, A hierarchical porous carbon aerogel embedded with small-sized TiO_2 nanoparticles for high-performance Li-S batteries, *Carbon*, 2023, **202**, 59–65.
50 S. Imtiaz, Z. Z. Ali, R. Razaq, *et al.*, Electrocatalysis on Separator Modified by Molybdenum Trioxide Nanobelts for Lithium-Sulfur Batteries, *Adv. Mater. Interfaces*, 2018, **5**(15), 1800243.
51 M. Yu, W. Yuan, C. Li, *et al.*, Performance enhancement of a graphene-sulfur composite as a lithium-sulfur battery electrode by coating with an ultrathin Al_2O_3 film via atomic layer deposition, *J. Mater. Chem. A*, 2014, **2**(20), 7360.
52 Y. Wu, C. Ye, L. Yu, *et al.*, Soft template-directed interlayer confinement synthesis of a Fe-Co dual single-atom catalyst for Zn-air batteries, *Energy Storage Mater.*, 2022, **45**, 805–813.
53 Z. Li, P. Li, X. Meng, *et al.*, The Interfacial Electronic Engineering in Binary Sulfiphilic Cobalt Boride Heterostructure Nanosheets for Upgrading Energy Density and Longevity of Lithium-Sulfur Batteries, *Adv. Mater.*, 2021, **33**(42), 2102338.
54 B. Wang, L. Wang, D. Ding, *et al.*, Zinc-Assisted Cobalt Ditelluride Polyhedra Inducing Lattice Strain to Endow Efficient Adsorption-Catalysis for High-Energy Lithium-Sulfur Batteries, *Adv. Mater.*, 2022, **34**(50), 2204403.
55 X. Zhou, G. Li, Y. Yu, *et al.*, Building Organic-Inorganic Robust Interphases from Deep Eutectic Solution for Highly Stable Mg Metal Anode in Conventional Electrolyte, *Small Methods*, 2023, 2301109.
56 W. Bao, L. Liu, C. Wang, *et al.*, Facile Synthesis of Crumpled Nitrogen-Doped MXene Nanosheets as a New Sulfur Host for Lithium-Sulfur Batteries, *Adv. Energy Mater.*, 2018, **8**(13), 1702485.